H and EUV observations of a partial CME

Christian, D. J., Jess, D. B., Antolin, P., & Mathioudakis, M. (2015). H and EUV observations of a partial CME. The Astrophysical Journal, 804(2). DOI: 10.1088/0004-637X/804/2/147

Published in:
The Astrophysical Journal

Document Version:
Publisher's PDF, also known as Version of record

The Astrophysical Journal, 804:147 (9pp), 2015 May 10 doi:10.1088/0004-637X/804/2/147

Hα AND EUV OBSERVATIONS OF A PARTIAL CME

Damian J. Christian[1], David B. Jess[2], Patrick Antolin[3], and Mihalis Mathioudakis[2]
[1] Department of Physics and Astronomy, California State University Northridge, 18111 Nordhoff Street, Northridge, CA 91330, USA; daman.christian@csun.edu
[2] Astrophysics Research Centre, School of Mathematics and Physics, Queen's University Belfast, Belfast, BT7 1NN, Northern Ireland, UK
[3] National Astronomical Observatory of Japan, 2-21-1 Osawa, Mitaka, Tokyo 181-8588, Japan
Received 2014 August 4; accepted 2015 March 10; published 2015 May 12

ABSTRACT

We have obtained Hα high spatial and time resolution observations of the upper solar chromosphere and supplemented these with multi-wavelength observations from the *Solar Dynamics Observatory* (*SDO*) and the *Hinode* Extreme-ultraviolet Imaging Spectrometer. The Hα observations were conducted on 2012 February 11 with the Hydrogen-Alpha Rapid Dynamics Camera instrument at the National Solar Observatory's Dunn Solar Telescope. Our Hα observations found large downflows of chromospheric material returning from coronal heights following a failed prominence eruption. We have detected several large condensations ("blobs") returning to the solar surface at velocities of $\approx$200 km s^{-1} in both Hα and several *SDO* Atmospheric Imaging Assembly band passes. The average derived size of these "blobs" in Hα is 500 by 3000 km^2 in the directions perpendicular and parallel to the direction of travel, respectively. A comparison of our "blob" widths to those found from coronal rain, indicate that there are additional, smaller, unresolved "blobs" in agreement with previous studies and recent numerical simulations. Our observed velocities and decelerations of the "blobs" in both Hα and *SDO* bands are less than those expected for gravitational free-fall and imply additional magnetic or gas pressure impeding the flow. We derived a kinetic energy of $\approx$2 orders of magnitude lower for the main eruption than a typical coronal mass ejection, which may explain its partial nature.

Key words: Sun: chromosphere – Sun: corona – Sun: coronal mass ejections (CMEs) – Sun: filaments, prominences

Supporting material: animation

1. INTRODUCTION

Building on the success of studies using the *Solar and Heliospheric Observatory* and TRACE, the *Solar Dynamics Observatory* (*SDO*) has uncovered a wealth of new information surrounding the magnetic structuring of the solar atmosphere. These magnetic features, including coronal loops, are found to be especially dynamic, often displaying eruptions related to emerging magnetic flux ropes. The emergent flux manifests itself as ribbons, loops, and strands (Moore & Sterling 2006), and is sometimes accompanied by eruptive events and coronal mass ejections (CMEs). Higher spatial resolution observations of the small-scale structures that arise in the aftermath of CME events, including those related to coronal rain, offer a unique ability to constrain and understand the dynamic processes embedded within the coronal magnetic fields.

Flares observed with CMEs have been noted as "eruptive" or "full eruptive" events, and flares with no CMEs have been noted as "confined" or "failed" (Wang & Zhang 2007; Kuridze et al. 2013). In a full CME, the plasma and associated magnetic structure is ejected and escapes from the Sun, while in a failed CME the plasma does not escape and falls back (Gilbert et al. 2007; Mrozek 2011). More recent observations have found that, regardless of whether the CME is a "full" or "failed" event, some material from the filament/prominence is often observed returning back to the solar surface (Innes et al. 2012; Gilbert et al. 2013). Gilbert et al. (2007) also define a "partial" filament eruption with two classes, A and B. The class A partial eruption has an eruption of the entire magnetic structure with a small amount of mass. Only part of the magnetic structure is observed to erupt in class B, also with a small amount of mass. Mrozek (2011) reviews several of the mechanisms, other than solar gravity, that can explain failed CMEs.

Recent observational studies of CMEs have found behavior and activity that can be interpreted by "tether cutting," "magnetic reconnection," or MHD kink instability scenarios. There are even instances where more than one of the scenarios are needed to explain the observations (Williams et al. 2005). Raftery et al. (2010) found support for the "tether-cutting" mechanism using multi-spaceraft X-ray observations of a C8 class flare plus CME. Recently, Bi et al. (2013) found rotation and non-radial motion during an eruptive filament. Many previous studies also found evidence for magnetic reconnection (Moore et al. 2001; Gary & Moore 2004; Joshi et al. 2007; Shen et al. 2012). Additionally, Kumar & Innes (2013) found evidence for blast waves leading to the break-out of the flux rope after magnetic reconnection, while Tripathi et al. (2007) also observed magnetic reconnection inside an emerging flux rope for a bright coronal downflow after a CME. There is also a heated debate on whether or not the magnetic flux rope exists before the onset of the CME or is formed during the process (Patsourakos et al. 2013).

Although failed CMEs have been poorly studied, Ji et al. (2003) found evidence for magnetic reconnection in a failed eruption, and Shen et al. (2012) used multi-angle observations of several failed eruptions to ascribe failed eruptions to several factors, including stronger magnetic field at low altitudes, low magnetic field gradients of the overlying loops with height, asymmetric magnetic confinement of the overlying fields, and the kinetic energy of the erupting filament mass. Within the class of chromospheric material falling back to the solar surface from coronal heights it is important to distinguish prominence material from coronal rain, which consists of cool plasma

condensation rapidly produced from thermal instability in the corona (in a timescale of minutes), falling toward the solar surface along coronal loops (Kawaguchi 1970; Leroy 1972; Schrijver 2001; De Groof et al. 2004, 2005). Coronal rain condensations can have velocities over 100 km s^{-1}, with typical velocities of 60–70 km s^{-1} (Antolin et al. 2010, 2012; Antolin & Rouppe van der Voort 2012; Kleint et al. 2014), and have been observed to cool very rapidly from coronal to chromospheric temperatures (Antiochos et al. 1999). There have been several investigations into the agents responsible for the less than free-fall speed observed in the rain, such as gas pressure (Müller et al. 2003, 2005; Antolin et al. 2010; Oliver et al. 2014), and ponderomotive force from transverse MHD waves (Antolin & Verwichte 2011). High temporal and spatial resolution observations of failed CMEs and coronal rain are needed to help distinguish between these different models and scenarios, and promise to help constrain parameters of the solar atmosphere, such as magnetic field strength, gradient, and plasma density.

In the current paper, we present new Hα observations showing large downflows of chromospheric material returning from coronal heights following a failed prominence eruption. These observations were conducted in 2012 February with the new Hydrogen-Alpha Rapid Dynamics camera (HARDcam; Jess et al. 2012) instrument and the National Solar Observatory's Dunn Solar Telescope. We supplemented our optical observations with EUV data obtained with the *SDO*'s Atmospheric Imaging Assembly (AIA) and the *Hinode* Extreme-ultraviolet Imaging Spectrometer (EIS). Our observations, and analysis are presented in Section 2. Our results are given in Section 3 and discussed in Section 4, with concluding remarks presented in Section 5.

2. OBSERVATIONS AND DATA ANALYSIS

2.1. Observations

2.1.1. Ground-based: HARDcam

The high velocities and relatively small structures in coronal loops require observations with high temporal and spatial resolution and these have only recently been achieved with newer rapid read-out ground-based camera systems, and high order adaptive optics for image reconstruction. We obtained observations of the solar limb at 32 N and 85.5 E on 2012 February 11 in two sequences at 16:11 and 16:21 UT with the new Hα camera HARDcam (Jess et al. 2012) at the Dunn Solar Telescope. HARDcam was run in conjunction with the Rapid Oscillations in the Solar Atmosphere (ROSA, Jess et al. 2010) camera system, which was observing photospheric bands that were not used in the present work. Our limb observations were conducted as part of our program to observe solar flares (DST proposal number T926), and, although we missed the flare near the solar limb, we detected several condensations ("blobs") returning to the solar surface.

The HARDcam (Jess et al. 2012) camera is an electron-multiplying CCD, with a quantum efficiency exceeding 95% at 6500 Å and is the Andor Technology model iXon X3 DU-887-BV. HARDcam has 512 × 512 pixels and was set-up with a spatial sampling of 0.138 arcsec per pixel, providing a field of view of 71″ × 71″. HARDcam was used with a 0.25 Å Hα core filter and triggered at a constant cadence of 0.05 s.

All data were obtained using real-time adaptive optics to correct distortions to the wave front and correct the seeing (Rimmele 2004). Further improvements were applied to the images in processing with speckle reconstruction (Weigelt & Wirnitzer 1983; Wöger et al. 2008) and Hα images were combined from 35 → 1, providing a final image cadence equal to 1.78 s. Images of our two Hα sequences are shown in Figure 1.

2.1.2. SDO AIA

We have supplemented our Hα observations with EUV images from the AIA (Lemen et al. 2011) on board the *SDO* (Pesnell et al. 2012). The AIA instrument images the entire solar disk in 10 different channels, incorporating a two-pixel spatial resolution of 1.″2 (≈900 km for the AIA's PSF) and a cadence of 12 s for the EUV channels and 24 s for the 1600 Å channel. Here, we selected five EUV data sets spanning 15:00–17:00 UT on 2012 February 11, consisting of 600 images in each of the 94, 171, 193, and 304 Å channels and 300 images for the 1600 Å channel. The *SDO* observations caught an eruption starting at ≈15:55 UT and the subsequent material returning to the solar surface. The main eruption stops its outward expansion and starts to fall back to the solar surface at ≈16:11. A smaller eruption is observed to the southeast and starts at ≈16:11 and then returns to the solar surface at ≈16:17. GOES detected a C2.7 flare just after 15:55 UT and a CME was observed by LASCO C2 at 16:48 UT, but was noted as a "poor event." A sample of images from several *SDO* bandpasses and our Hα data are shown in (Figure 2) near the time of the onset of a selected "blob" in Hα, and a movie, M1 is provided in the online material for the Hα, and *SDO* AIA 1600, 304, and 171 Å data sets. Image sequences for the 304 and 1600 Å bandpasses are also shown in Figure 3 with selected features noted and also presented in Table 1.

2.1.3. Hinode/EIS

Observations from EIS (Culhane et al. 2007) of the *Hinode* satellite (Kosugi et al. 2007) during the time of our HARDcam observations are also included. In Figures 4 and 5, we show EIS data at the wavelength of Fe XII 195.12 Å, formed at a temperature of log T = 6.2. The data were reduced using standard EIS software included in the SolarSoft package (Freeland & Handy 1998). The slot image corresponds to a 40″ slot reconstruction at 15 adjacent positions, leading to an entire field of view of 487 × 487 $arcsec^2$, and was taken at 17:11:47 UT on 2012 February 11. The slit carried out sit-and-stare observations in Fe XII 186.74 and 195.12, and Fe XVI 262.98, throughout the day in tracking mode with a cadence of 23.8 s. Most of the slit was off-limb throughout the observations, as shown in the context slot figure. The calculation of the moments for the slit data was carried out using the eis_auto_fit routine, which automatically takes care of the spectrum drift and the slit tilt using the method described by Kamio et al. (2010). Kamio et al. (2010) estimate that this method provides an accuracy of ±4.4 km s^{-1}. On the other hand, the line profiles over the region of interest (off-limb) retain a Gaussian shape throughout the observations and, therefore, we believe single Gaussian fits to the data provide good estimates of the line widths regardless of the absolute centroid for Fe XII 195.12 Å. In Figure 5, we show spacetime diagrams for the intensity, Doppler velocity, and line width for the Fe XII 195.12 Å line, for the time interval of 15:12:0–17:10:30 UT. The other two lines require longer

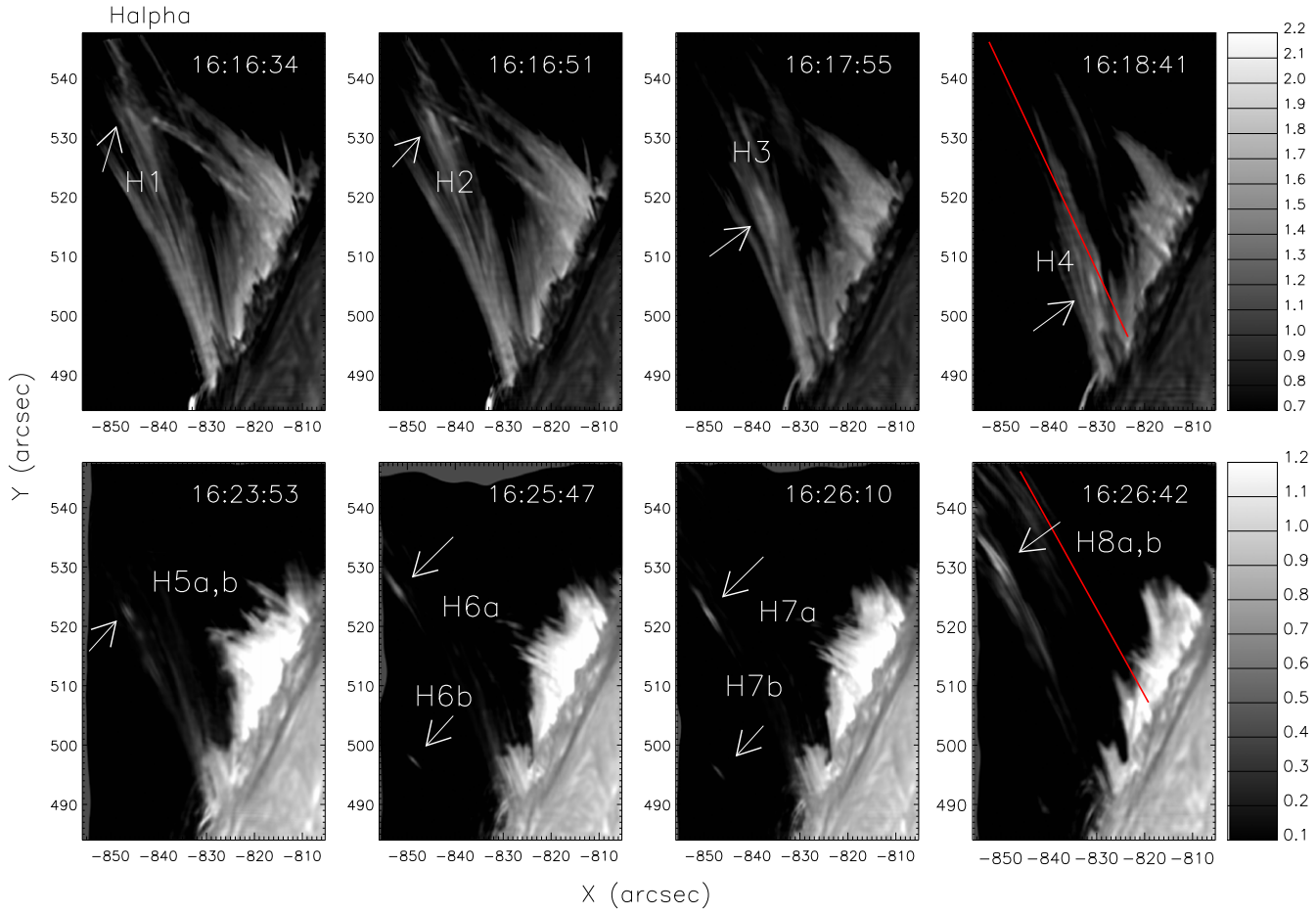

Figure 1. HARDcam Hα images from 2012 February 11 showing blobs of material falling back toward the solar surface (see the text). The top panel shows selected images for the first image sequence starting at 16:11:24 UT (series 1) and the lower panel shows selected images from the second sequence starting at 16:21:42 UT (series 2). Features of selected blobs can be found in Table 1. The lower right panels for each Hα sequence also shows the trace for the X–T cuts used in Figure 6.

exposure times for proper signal-to-noise and are, therefore, not included in the present study.

3. RESULTS

Our Hα observations detected many plasma condensations ("blobs") falling back toward the solar surface. We measured the condensation distances, velocities, and sizes from the best sequence of Hα images starting near 16:16:24 UT. The largest plasma condensation, or "blob," entered the HARDcam field at ~35,000 km from the solar limb at 16:16 UT. The average width (direction perpendicular to its motion) and length (direction parallel to its motion) blob sizes were 5 and 30 pixels, corresponding to physical sizes of ≈500 and 3000 km, respectively. This is larger than the typical sizes for coronal rain, a phenomena that will be further discussed in Section 4. Sample "blob" sizes (taken from Figure 1) are shown in Table 1.

We created spacetime cuts of the Hα images and found velocities of $196 \pm 10\,\mathrm{km\,s^{-1}}$ (Figure 6), derived from the slope of the maximum length of the track in the X–T plot. These values are at the higher end for typical velocities found for CMEs and in coronal rain (Tripathi et al. 2006, 2007; Antolin et al. 2010, 2012; Antolin & Rouppe van der Voort 2012; Innes et al. 2012; Patsourakos et al. 2013; Dolei et al. 2014; Xue et al. 2014). Velocities derived from the second set of Hα observations were found to be 209 ± 15 and $218 \pm 20\,\mathrm{km\,s^{-1}}$ for the top right spacetime cuts in Figure 6. The seeing becomes very poor near the end of the second set of Hα observations (near ≈16:28 UT), and this later interval of data and periods of poor seeing were not included in the velocity estimates. Kuridze et al. (2013) observed a failed CME with downward velocities of $60 \pm 10\,\mathrm{km\,s^{-1}}$ and Ji et al. (2003) found much higher typical velocities of $\approx 200\,\mathrm{km\,s^{-1}}$.

We also observed several plasma condensations or blobs returning toward the solar surface in *SDO* AIA 304 Å images (see Figure 3). The first blob during the Hα sequence appeared at ≈16:15 UT at a distance of ≈40,000 km above the solar surface. Its width and length were 7″ × 22″, corresponding to a physical size of ≈5000 by 17,000 $\mathrm{km^2}$. Three other condensations were also observed by *SDO* during the second HARDCam sequence, and had sizes slightly larger than the first, on the order of ≈7000 by 18,000 $\mathrm{km^2}$. In Table 1, we present a summary of the sizes of several of the condensation features (blobs) returning to the solar surface.

Velocities for the blobs were found to be ≈ 190–$200\,\mathrm{km\,s^{-1}}$ over the 10 minute sequence from 16:15 to 16:30 for the *SDO* AIA 304 Å bandpass. A velocity of $\approx 190 \pm 22\,\mathrm{km\,s^{-1}}$ was found for the first minute after the blob appeared at 16:17 UT and is in agreement with the velocities derived from the Hα observations. The derived velocities are affected by the large cadence time of 12 s and poorer spatial resolution of the *SDO*. The *SDO* 1600 Å band had a similar structure to the Hα images

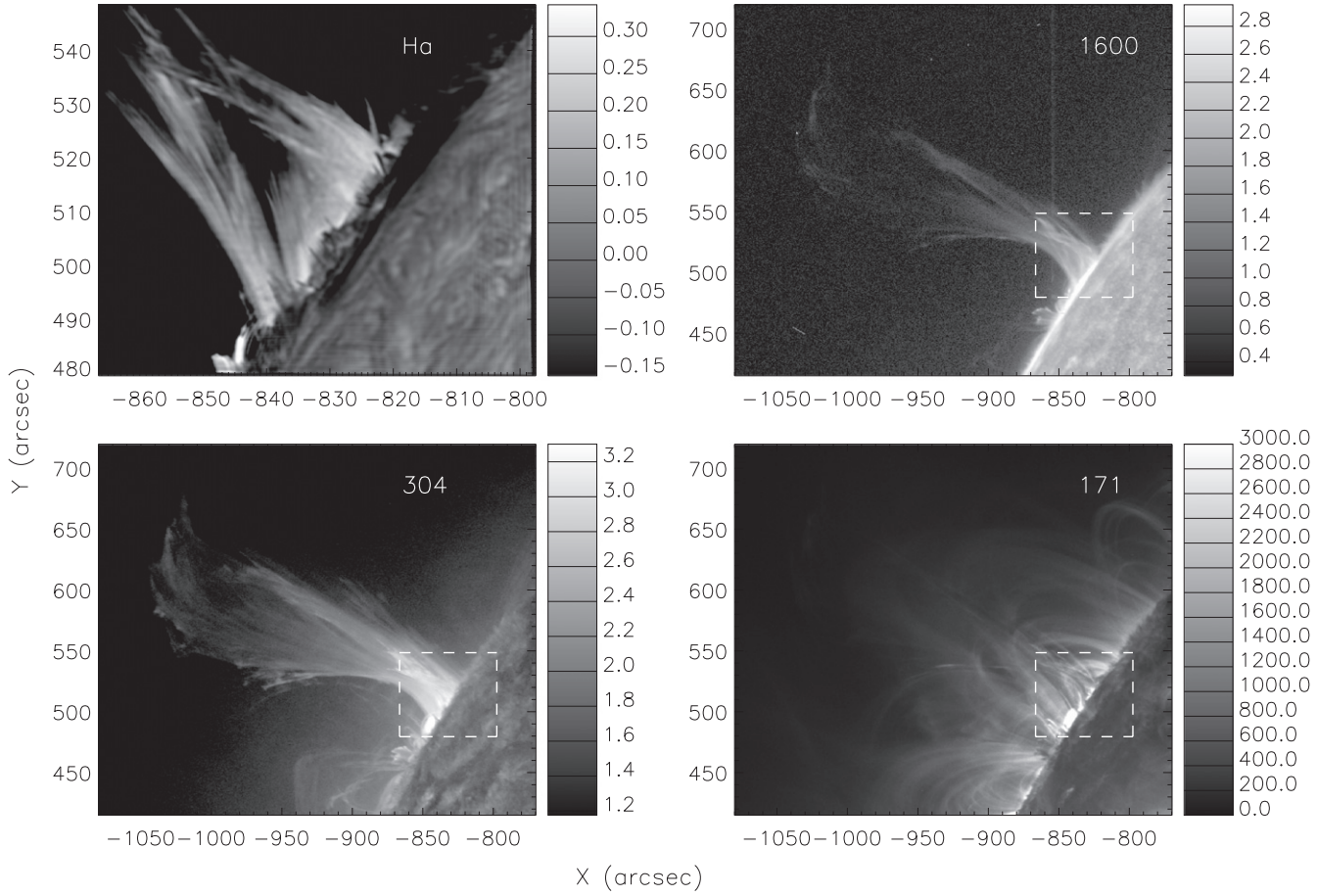

Figure 2. HARDcam Hα and *SDO* AIA sample images from Movie 1 in the online material. The images are taken near 16:16:50 UT. Shown are the Hα HARDcam data in the upper left panel and *SDO* AIA 1600, 304, and 171 Å bands in the upper right and lower left and right panels, respectively. All images are displayed using a log scale and the HARDcam field of view is indicated in the *SDO* images as the white box. In the movie, the *SDO* data spans from 15:00 to 17:00 UT and the HARDcam data from ≈16:11 to 16:30, and black frames are shown for the times where there were no HARDCam observations.

(An animation of this figure is available.)

and velocities of falling blobs ranged from 180–210 km s^{-1}, though the same blobs were not matched for both data sets. This may be the result of different temperatures and opacities observed in each band pass and some information may be lost as a result of the 24 s cadence in the 1600 Å band.

The start of the eruption, as seen in the *SDO* AIA i filters, is marked in Figure 5, the spacetime diagrams, as a dashed line for the *Hinode*/EIS observations. Line widths observed with *Hinode*/EIS show an increase of Doppler shifts throughout the slit a few minutes later. Clear changes of Doppler shifts, from redshifts of +5 km s^{-1} to blueshifts of −5 km s^{-1} are observed all along the slit for both the off-limb and the on-disk regions. Such relatively strong changes over a distance of over 500″ along the solar surface suggest a large-scale reconfiguration of the magnetic field caused by the eruption. Particularly, in the slit range above 550″, we notice a dimming region in the intensity images, co-located to relatively strong variations of the Doppler shifts, from +10 km^{-5} to −10 km^{-5} over a time interval of 15 min. Within this interval, and also co-located, we observe strong variations in line width with shifts from 40 to 70 km s^{-1} over short intervals of 5 min. Despite the poor signal-to-noise, an increase in the Fe XII 186.74 line width is also observed in the same spatial and temporal locations. The time interval in which these variations are observed corresponds to the first part of the eruption, lasting 40 min in which most of the material is seen going upward. Correspondingly, the erupting material appears in emission in the cool AIA filters such as 304 and 1600 Å but appears in absorption in the 193 Å filter, matching the dimming observed in the EIS Fe XII line. In the second part of the eruption, lasting 40 min in which material is seen to fall back to the solar surface, the Fe XII 195 line intensity is gradually increased and the Doppler velocity shows smaller variations of a few km s^{-1} around the rest wavelength. Gradually over this 40 min interval the flows turn into constant redshifts of +5 km s^{-1}, the same values prior to the eruption. The line width on the other hand decreases sharply from its maximum value in a time interval of 10 minutes and retains henceforth the same pre-eruption values of 40 km s^{-1}.

The sharp changes in line width are probably mainly caused by a non-thermal component, since no abrupt temperature increase is observed in Fe XII 195. Furthermore, the Doppler velocity also displays a significant change over the same time interval, supporting this scenario. A close inspection to the AIA filters, especially the 304 filter, shows regions exhibiting both upward and downward flowing material over short intervals of time, and also transverse swaying. These dynamics can very well explain the increase in line width.

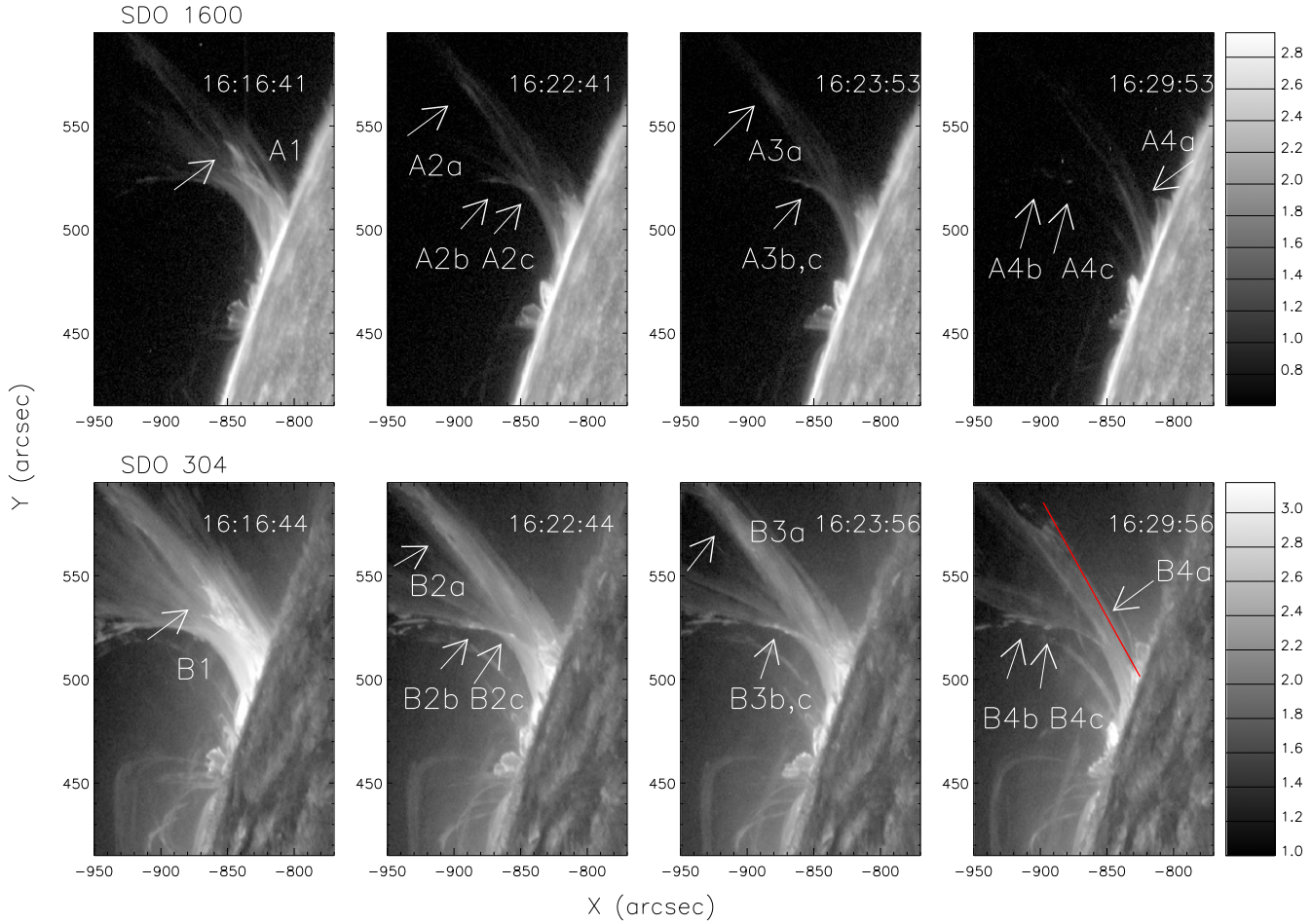

Figure 3. *SDO* AIA sequence of images from 2012 February 11 (near 16:16 UT) showing selected features ("blobs") of interest. The 1600 and the 304 Å bands are shown in the top and bottom panels, respectively. Properties of these blobs are given in Table 1. The lower right panel for the *SDO* 304 Å image sequence also shows the trace for the X–T cuts used in Figure 6.

4. DISCUSSION

Failed CMEs, when the plasma does not escape from the Sun, promise to provide constraints on the physical parameters of the corona and upper chromosphere. We have detected the phenomenon of plasma returning to the solar surface in the aftermath of a failed CME. These features were detected in high resolution Hα observations of the solar limb, in addition to contemporaneous *SDO*/AIA data. The *SDO* observations also observed the eruption, which we classify as a failed prominence eruption, since prominence material being ejected from the Sun is not common in surges, sprays, or jets.

4.1. Free-fall Velocities

Antolin & Rouppe van der Voort (2012), using the CRisp Imaging SpectroPolarimeter (CRISP) in the Hα band studied a large sample of blobs and found typical widths and lengths of 300 and 700 km, respectively. Our blobs (condensation features) are two and five times larger in width and length, respectively. This implies that our blobs are not coronal rain, but more likely a failed or partly failed CME. Spacetime cuts of the *SDO* AIA 304 Å band found CME out-bond velocities of 200–300 km s^{-1}, which are consistent with CME velocities in the lower corona at distances less than 1 $R_\odot$ (Patsourakos et al. 2013). Our observed in-falling velocities range from 190 to 220 km s^{-1} for our Hα observations and ≈180–210 km s^{-1}, for the *SDO* 304 and 1600 Å bands.

The expected free-fall velocity can be given by

$$v_{\rm ff} = \sqrt{\frac{2GM_\odot h_{\rm max}}{R_\odot\left(R_\odot + h_{\rm max}\right)}}, \quad (1)$$

where $M_\odot$ is the mass of the Sun, $R_\odot$ is the Sun's radius, and $h_{\rm max}$ is the maximum loop height (Müller et al. 2005). From our sequence of HARDcam images, we find $h_{\rm max}$ to be about 350 pixels, or ≈35,000 km, and to result in an expected free-fall velocity using the above equation of 135 km s^{-1}. However, for the much larger *SDO* field of view, we find $h_{\rm max}$ to be ≈180,000 km, and this corresponds to a free-fall velocity of 280 km s^{-1}. If the plasma observed in Hα originated from these heights, then we would expect it to reach a free-fall velocity of ≈280 km s^{-1}. We measure an inclination for blobs observed returning to the solar surface in our sequence 1 to be falling at ≈25° to the solar normal and ≈15–20° in sequence 2. We also note that any inclination of the guiding magnetic field to the normal to the solar surface would lower the effective gravitational acceleration. There is also the unknown inclination of the material to the observer's line of sight, and this

Table 1
Sample Condensation Features

Feature	Time (UT)	Size (km^2)	Feature	Time (UT)	Size (km^2)	Feature	Time (UT)	Size (km^2)	Comments[a]
	Hα			AIA 1600 Å			AIA 304 Å		
H1	16:16:34	700 × 1300	A1	16:16:41	2350 × 9960	B1	16:16:44	1090 × 9000	⋯
H2	16:16:51	730 × 2900	A2a	16:22:41	1830 × 8480	B2a	16:22:44	2910 × 9050	⋯
			A2b	16:22:41	4180 × 2700	B2b	16:22:44	2610 × 1830	horiz.
			A2c	16:22:41	1090 × 3050	B2c	16:22:44	1600 × 3600	⋯
H3	16:17:55	770 × 4340	A3a	16:23:53	2910 × 9270	B3a	16:23:56	1670 × 10530	⋯
			A3b	16:23:53	1440 × 1780	B3b	16:23:56	1610 × 1520	⋯
			A3c	16:23:53	1300 × 2180	B3c	16:23:56	1440 × 2130	⋯
H4	16:18:41	500 × 2340	A4a	16:29:53	1650 × 13880	B4a	16:29:44	1830 × 6310	⋯
			A4b	16:29:53	4390 × 2570	B4b	16:29:44	3610 × 1520	horiz.
			A4c	16:29:53	2570 × 1220	B4c	16:29:44	1610 × 870	horiz.
H5a	16:23:53	410 × 2620	⋯	⋯	⋯	⋯	⋯	⋯	⋯
H5b	16:23:53	410 × 2790	⋯	⋯	⋯	⋯	⋯	⋯	
H6a	16:25:47	1260 × 4900	⋯	⋯	⋯	⋯	⋯	⋯	2 blobs
H6b	16:25:47	470 × 2300	⋯	⋯	⋯	⋯	⋯	⋯	⋯
	Hα	⋯	⋯	⋯	⋯	⋯	⋯	⋯	⋯
H7a	16:26:10	1170 × 6900	⋯	⋯	⋯	⋯	⋯	⋯	2 blobs
H7b	16:26:10	410 × 1740	⋯	⋯	⋯	⋯	⋯	⋯	⋯
H8a	16:26:42	590 × 3450	⋯	⋯	⋯	⋯	⋯	⋯	⋯
H8b	16:26:42	340 × 5330	⋯	⋯	⋯	⋯	⋯	⋯	⋯
H9a	16:27:50	830 × 4600	⋯	⋯	⋯	⋯	⋯	⋯	⋯
H9b	16:27:50	340 × 5600	⋯	⋯	⋯	⋯	⋯	⋯	⋯

[a] Comments: horiz. = a horizontal feature in *SDO*; 2 blobs = evidence for two unresolved blobs.

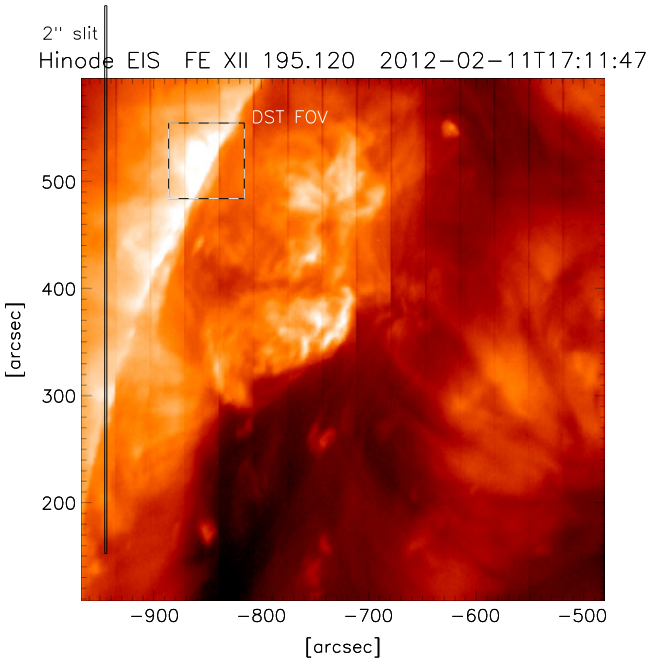

Figure 4. *Hinode*/EIS Fe XII 195.12 Å image. The location of the DST field of view (white square) as well as that of the EIS 2″ slit is shown.

would imply that we only observe a lower limit to the actual velocity.

Our first (series 1) and second (series 2) sequences of Hα observations find free-fall velocities that are ≈20%–30% lower than those expected from gravity alone. Correcting for the small inclination angle between the returning material and the observer's line of sight decrease this disparity, but it still remains at 10%–20%. The observed velocities at values lower than the those expected from gravitational free-fall are in agreement with coronal rain observations (Schrijver 2001; De Groof et al. 2004, 2005; Müller et al. 2005; Antolin et al. 2010; Antolin & Rouppe van der Voort 2012), where average blob accelerations are one-third or less than solar gravity. Interpretations have been provided in terms of gas pressure variation from upward propagating slow modes (Antolin et al. 2010) or pressure restructuring by slow modes produced by the blobs themselves. For the latter, slow mode shocks would travel down restoring the gas pressure and make the blobs fall at constant speeds (Oliver et al. 2014).

Ji et al. (2003) observed a maximum free-fall velocity of material returning to the solar surface after a failed filament eruption of nearly 300 km s^{-1} and found a maximum deceleration of this material of 10 times $g_\odot$ and interpret this force as magnetic tension. The material that we observed returning to the solar surface has a maximum velocity of ≈255 km s^{-1}, and we find typical decelerations of the falling blobs of 2–3 $g_\odot$ with a maximum of ≈12 $g_\odot$ from the velocities presented in Figure 7. These velocities and decelerations were derived from measuring the slope along the main track in the X–T plot (Figure 6) at ≈7 s intervals. These decelerations are similar to those found by Ji et al. (2003), but we caution that there is a large amount of scatter in the velocity measurements, there is an unknown inclination to the observer's line of sight, and the uncertainties may be large.

4.2. Condensation Parameters

Condensations (blobs) returning to the solar surface are first observed at over ≈180,000 km above the solar surface in both the 304 and 1600 Å bandpasses. The 1600 Å continuum bandpass is dominated by emission from C IV with a temperature of about 10^5 K. The 304 Å channel is sensitive to

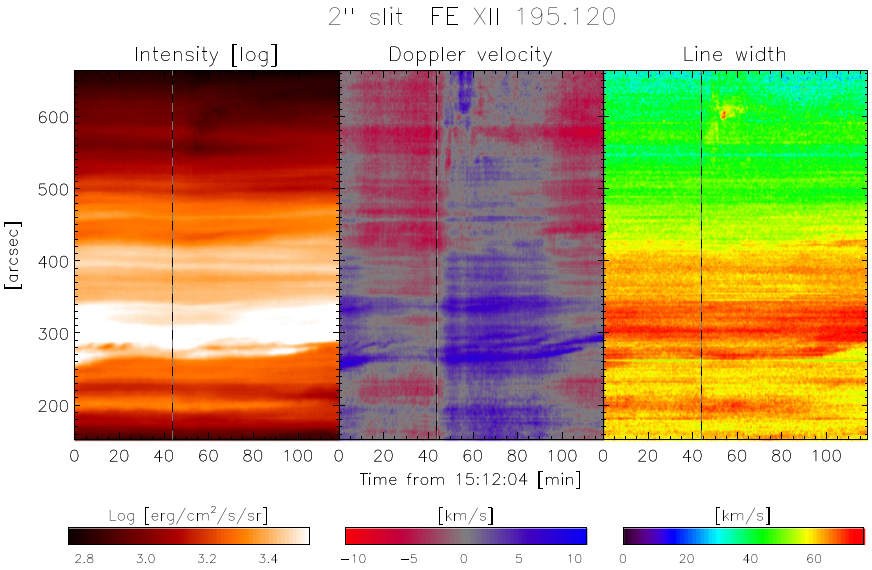

Figure 5. *Hinode*/EIS data (from left to right) for spacetime diagrams for the intensity, Doppler velocity, and line width for the Fe XII 195.12 line, for the time interval of 15:12:04 to 17:10:30 UT. The zero point of the Doppler velocity is set from the average for a small region of 5 arcsec at the bottom of the slit where no activity was observed, and restricted to 45 minutes before the eruption. The start of the eruption, as seen in the AIA filters, is marked in all panels as a vertical dashed line, and the largest changes after the eruption are seen above the 550″ slit position.

He II emission at $\approx 5 \times 10^4$ K; however, the off-limb emission can be dominated by Si XI emission with a temperature of 1.6×10^6 K (O'Dwyer et al. 2010). This material is detected at ≈35,000 km above the solar surface in the Hα band (temperature $\approx 10^4$ K). Although similar structures are observed in the 1600 Å and Hα bandpasses (see Figure 2 and Movie 1), we were unable to match blobs in the different bandpasses. This may be a result of both the very different temperatures in the different bands and the spatial and temporal sampling.

Our Hα observations have only detected ≈50 blobs returning to the solar surface that are over 2σ significance above the median intensity (the parameters for a sample of these are presented in Table 1). We find that there is not so much clumpy structure in our observations. Antolin & Rouppe van der Voort (2012) detected nearly 4000 blobs returning to the solar surface in the CRISP observations of both on-disk and off-disk coronal rain and found a mean width for their distribution for on-disk coronal rain of 310 km. We have computed a similar distribution for our Hα observations and find an average width of about 530 km. We compare these two Hα size distributions in Figure 8. Our larger average sizes are consistent with our factor of ≈2 larger resolution. We also note, as did Antolin & Rouppe van der Voort (2012), that there may be many more unresolved structures, and the slight rise to smaller "blob" widths in our distribution supports this. The structure observed in coronal rain may form as the result of thermal instabilities and blob sizes may provide further constrains on the detailed physics of eruptions and coronal rain (Ofman & Thompson 2011; Oliver et al. 2014). Fang et al. (2013) simulated 4000 "blobs" returning to the solar surface in an 80 minute period and found an average width of 400 km, and note that only about 25% of these blobs would be detectable with the current instrumental resolution. Such a "blob" distribution is consistent with our Hα observations.

4.3. Failed CME Kinetic Energy

The main outburst observed in the *SDO* bands started at ≈15:55 UT and it was also accompanied by a strong increase in Doppler shifts (20 km s^{-1} change from the start of the eruption) and a strong increase in line width (from 40 to 70 km s^{-1}) as observed by the *Hinode*/EIS. We approximate the extent of the area of the CME at 16:06 UT as a triangular shape of 6000 x 25300 km^2. Assuming that its thickness is equal to its width, we find a volume of 2.4×10^{11} km^3 and this gives a mass of $\approx 4.0 \times 10^{11}$–$10^{13}$ g for an estimated range of densities of 10^9–10^{11} cm^{-3} spanning values for typical densities in prominences to flares (Hirayama 1985; O'Dwyer et al. 2010). This mass gives a maximum kinetic energy in the main eruption of $\approx 2 \times 10^{28}$ ergs for a velocity of 300 km s^{-1}, much smaller than a typical large CME (Forbes 2000). These values are two orders of magnitude lower than the typical CME masses of 10^{15}–10^{16} g (Gilbert et al. 2007). This low kinetic energy may explain why this is a partial CME (e.g., Shen et al. 2011). We now derive masses of our of typical blobs using a volume from the average blob size 500 × 3000 km^2 and assuming a thickness equal to our measured 500 km width, and an average density, gives masses of $\approx 1.3 \times 10^{10}$ g. Such a blob would have a kinetic energy of $\approx 5.0 \times 10^{24}$ ergs for this average mass, and this is also several orders of magnitude smaller than those found from typical CMEs (Forbes 2000). Additionally, if we sum up the masses of the ≈50 individual blobs (including those presented in Table 1), $\rho \sum_{i=1}^{n} m_i$, we find a total mass of $\approx 5.0 \times 10^{11}$ g for an average density of 10^{10} cm^{-3}. This implies that only about 18% of the material returns to the solar surface as compared to our estimated mass in the main outburst. If we have detected only about half of the blobs returning to the solar surface, then the total mass is still less the 36% of the initial CME and the majority of mass escapes from the Sun. Our *SDO*, Hα, and *Hinode*/EIS observations of this failed CME support the suggestion that the outburst observed is consistent with a partial eruption as described in Gilbert et al. (2007), and only a

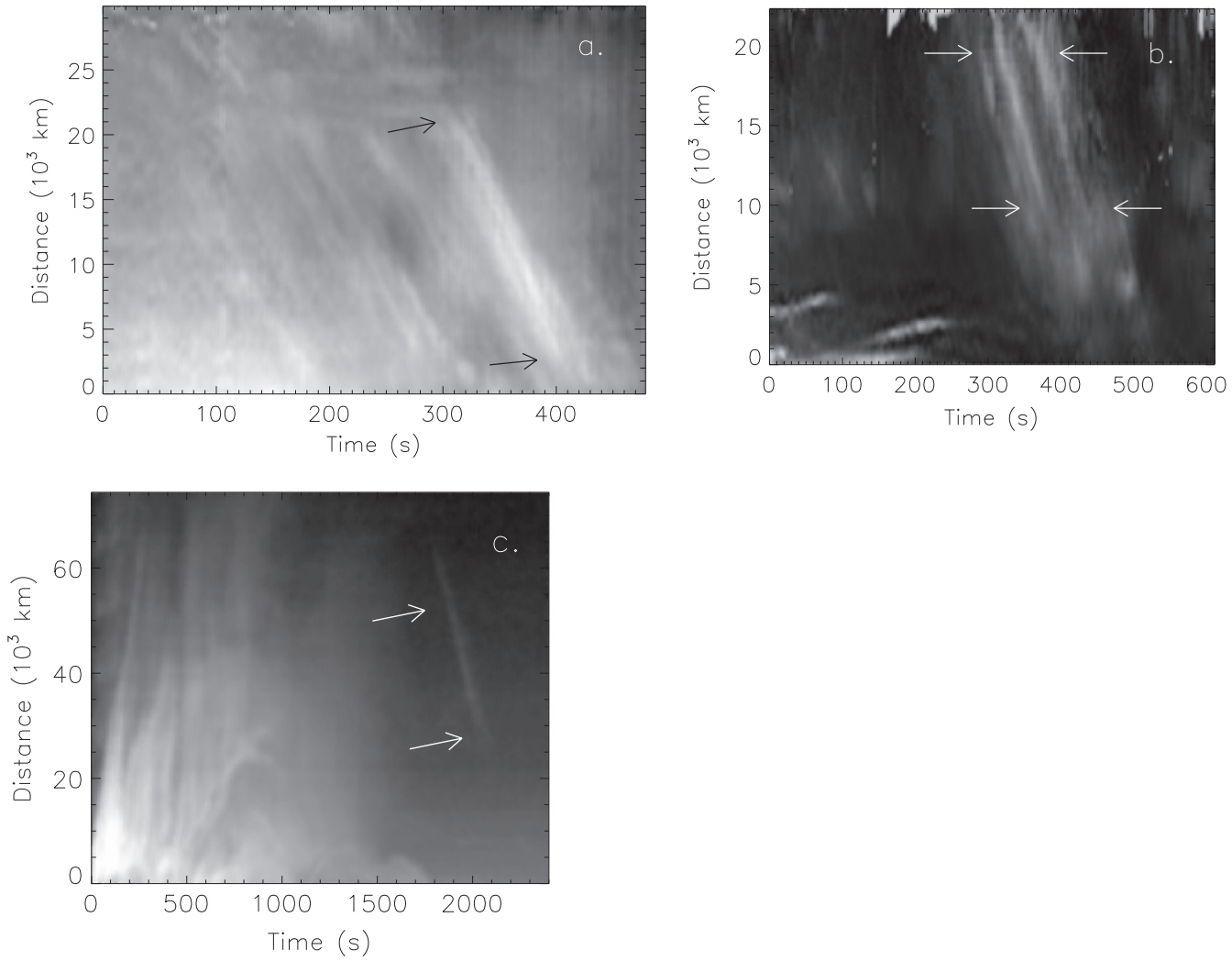

Figure 6. Spacetime plots in Hα and *SDO* 304 Å images from 2012 February 11 showing blobs falling back toward the solar surface. The top panels show the spacetime plots for Hα with (a) the left panel showing the spacetime plot for series 1 (UT 16:11:24 start time) and (b) the right panel showing the second series (start time UT 16:21:42). (c) The lower panel shows the spacetime plot of the *SDO* 304 Å band starting at UT 16:00 with a logarithmic intensity scale. Arrows indicate the region from which velocities were derived (see the text).

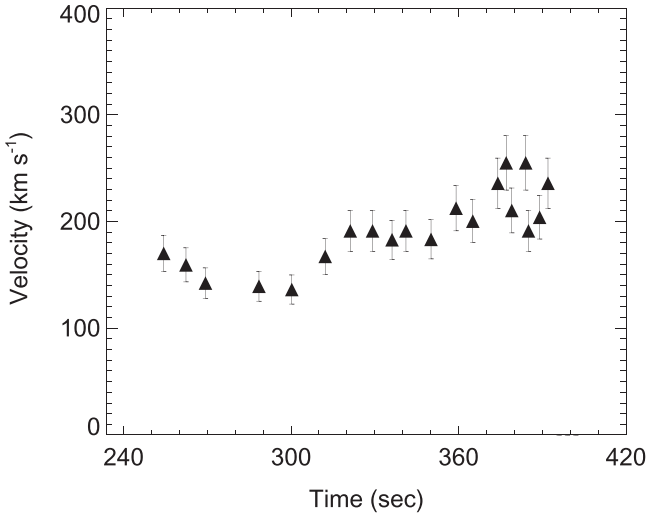

Figure 7. Hα velocity as a function of time for our first sequence of Hα observations (series 1) for the condensation H1, observed at 16:16:34 in the upper panel of Figure 1 and in the spacetime cuts in Figure 3.

fraction of the ejected mass returns to the solar surface in the form of blobs.

5. CONCLUDING REMARKS

We have used a multi-instrument, multi-wavelength approach to obtain high spatial and temporal resolution observations of the upper solar chromosphere and have detected condensations ("blobs") returning to the solar surface at velocities of $\approx$200 km s^{-1} after a failed prominence eruption. Velocities in the upper corona from *SDO* AIA images were in general agreement, but blobs could not be matched to the ones observed in Hα, probably as the result of very different temperature and opacity distributions, and also spatial and temporal sampling. Derived average "blob" sizes in Hα are $\approx$500 × 3000 km^2 in the directions perpendicular and parallel to the direction of travel, respectively and are much larger than sizes found for typical coronal rain. A comparison of our "blob" widths to those found from coronal rain, indicate that there are additional smaller, unresolved "blobs" in agreement with recent numerical simulations (Fang et al. 2013). We

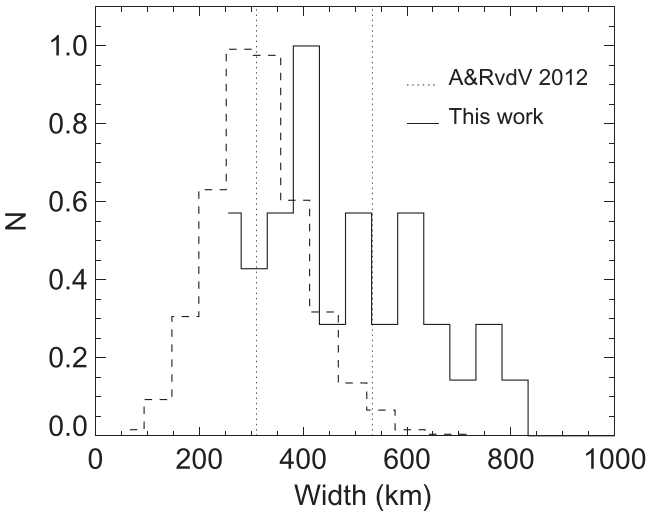

Figure 8. Normalized histograms for the widths of the condensation observed in Hα. The histogram adapted from Antolin & Rouppe van der Voort (2012) is shown as the dashed line (noted at A&RvdV) and has an average width of 310 km (indicated by the horizontal dotted line). The distribution of the Hα condensations measured in this work is shown as the solid line and has an average width of ≈530 km (indicated by the horizontal dotted line), owing to our larger resolution (see the text).

interpret our Hα and EUV observations as a partial CME. We derived a kinetic energy that is ≈2 orders of magnitude lower for the main eruption (at UT 15:55) than a typical CME, which may explain its partial nature. Our observed velocities and decelerations of the blobs in both Hα and *SDO* bands are less than those expected for gravitational free-fall and imply additional magnetic or gas pressure impeding the flow. However, we realize additional high spatial and temporal resolution observations of the solar limb are needed to quantify both failed CMEs and other phenomenon, which will allow further constraints on the coronal magnetic field and in the larger problem of coronal heating.

We thank D. Gilliam and all of the DST staff for their excellent support for this project. We also thank the anonymous referee for suggested improvements to this manuscript. D. C. dedicates this paper to his late mother, Rosemarie Sciortino Christian.

REFERENCES

Antolin, P., & Rouppe van der Voort, L. 2012, ApJ, 745, 152
Antolin, P., Shibata, K., & Vissers, G. 2010, ApJ, 716, 154
Antolin, P., & Verwichte, E. 2011, ApJ, 736, 121
Antolin, P., Vissers, G., & Rouppe van der Voort, L. 2012, SoPh, 280, 457
Antiochos, S. K., MacNeice, P. J., Spicer, D. S., & Klimchuk, J. A. 1999, ApJ, 512, 985
Antiochos, S. K., MacNeice, P. J., Spicer, D. S., & Klimchuk, J. A. 1999, ApJ, 633
Bi, Yi., Jiang, Y., Yang, J., et al. 2013, ApJ, 773, 162
Brooks, D. H., Warren, H. P., & Ugarte-Urra, I. 2012, ApJ, 755, 33
Culhane, J. L., Harra, L. K., James, A. M., et al. 2007, SoPh, 243, 19
De Groof, A., Bastiaensen, C., Müller, D. A. N., Berghmans, D., & Poedts, S. 2005, A&A, 443, 319
De Groof, A., Berghmans, D., van Driel-Gesztelyi, L., & Poedts, S. 2004, A&A, 415, 1141
Dolei, S., Bemporad, A., & Spadaro, D. 2014, A&A, 562, 74
Fang, X., Xia, C., & Keppens, R. 2013, ApJ, 771, 29
Forbes, T. G. 2000, JGR, 105, 23153
Freeland, S. L., & Handy, B. N. 1998, SoPh, 182, 497
Gary, G. A., & Moore, R. L. 2004, ApJ, 611, 545
Gilbert, H., Alexander, D., & Liu, R. 2007, SoPh, 245, 287
Gilbert, H. R., Inglis, A. R., Mays, M. L., et al. 2013, ApJ, 776, 12
Hirayama, T. 1985, SoPh, 100, 415
Innes, D. E., Cameron, R. H., Fletcher, L., Inhester, B., & Solanki, S. K. 2012, A&A, 540, 10
Jess, D. B., De Moortel, I., Mathioudakis, M., et al. 2012, ApJ, 757, 160
Jess, D. B., Mathioudakis, M., Christian, D. J., et al. 2010, SoPh, 261, 363
Ji, H., Wang, H., Schmahl, E. J., moon, Y.-J., & Jiang, Y. 2003, ApJL, 595, L135
Joshi, B., Manoharan, P. K., Veronig, A. M., Pant, P., & Pandey, K. 2007, SoPh, 242, 143
Kamio, S., Hara, H., Watanabe, T., Fredvik, T., & Hansteen, V. H. 2010, SoPh, 266, 209
Kawaguchi, I. 1970, PASJ, 22, 405
Kitiashvili, I. N., Kosovichev, A. G., Lele, S. K., Mansour, N. N., & Wray, A. A. 2013, ApJ, 770, 37
Kleint, L., Antolin, P., Tian, H., et al. 2014, ApJL, 789, L42
Kosugi, T., Matsuzaki, K., Sakao, T., et al. 2007, SoPh, 243, 3
Kumar, P., & Innes, D. E. 2013, SoPh, 208, 255
Kuridze, D., Mathioudakis, M., Kowalski, A. F., et al. 2013, A&A, 552, 55
Lemen, J. R., Title, A. M., Akin, D. J., et al. 2011, SoPh, 275, 17
Leroy, J. 1972, SoPh, 25, 413
Moore, R. L., Sterling, A. C., Hudson, H. S., & Lemen, J. R. 2001, ApJ, 552, 833
Moore, R. L., & Sterling, A. C. 2006, in Solar Eruptions and Energetic Particles ed. N. Gopalswamy, R. Mewaldt, & J. Torsti (Washington, DC: AGU), 43
Mrozek, T. 2011, SoPh, 270, 191
Müller, D. A. N., De Groof, A., Hansteen, V. H., & Peter, H. 2005, A&A, 436, 1067
Müller, D. A. N., Hansteen, V. H., & Peter, H. 2003, A&A, 411, 605
O'Dwyer, B., del Zanna, G., Mason, H. E., Weber, M. A., & Tripathi, D. 2010, A&A, 521, 21
Ofman, L., & Thompson 2011, ApJ, 734, 11
Oliver, R., Soler, R., Terradas, J., Zaqarashvili, T. V., & Khodachenko, M. L. 2014, ApJ, 784, 21
Patsourakos, S., Vourlidas, A., & Stenborg, G. 2013, ApJ, 764, 125
Pesnell, W. D., Thompson, B. T., & Chamberlin, P. C. 2012, SoPh, 275, 3
Raftery, C. L., Gallagher, P. T., McAteer, R. T. J., Lin, C.-H., & Delahunt, G. 2010, ApJ, 721, 1579
Rimmele, T. R. 2004, Proc. SPIE, 5490, 34
Schrijver, C. J. 2001, SoPh, 198, 325
Shen, Y.-D., Liu, Y., & Liu, R. 2011, RAA, 11, 594
Shen, Y., Liu, Y., & Su, J. 2012, ApJ, 750, 12
Tripathi, D., Solanki, S. K., Mason, S. E., & Webb, D. F. 2007, A&A, 472, 633
Tripathi, D., Solanki, S. K., Schwenn, R., et al. 2006, A&A, 449, 369
Wang, Y., & Zhang, J. 2007, ApJ, 665, 1428
Weigelt, G., & Wirnitzer, B. 1983, OptL, 8, 389
Williams, D. R., Török, T., Démoulin, P., van Driel-Gesztelyi, L., & Kliem, B. 2005, ApJL, 628, L163
Wöger, F., von der Lhe, O., & Reardon, K. 2008, A&A, 488, 375
Xue, Z., Yan, X., Qu, Z., & Zhao, L. 2014, NewA, 26, 23